Agricultural and Forest Meteorology 357 (2024) 110195

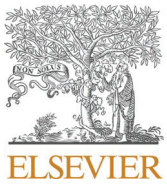

Contents lists available at ScienceDirect

Agricultural and Forest Meteorology

journal homepage: www.elsevier.com/locate/agrformet

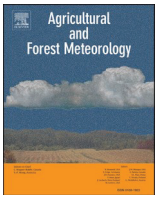

Are the ecosystem-level evaporative stress indices representative of evaporative stress of vegetation?

Pushpendra Raghav, Mukesh Kumar *

Department of Civil, Construction, and Environmental Engineering, University of Alabama, Tuscaloosa, AL, USA

ARTICLE INFO

Keywords:
Drought
Remote sensing
Agricultural drought
ESI
ESR
Evapotranspiration partitioning

ABSTRACT

Evaporative Stress Index (ESI), also sometimes referred as Evaporative Stress Ratio (ESR), has been widely used as an indicator of vegetation evaporative stress, and is often used to track forest and agriculture droughts. Lower the stress, higher is the value of ESI or ESR. The goal of this study is to assess the suitability of these indices for tracking vegetation evaporative stress. As the dynamics of water loss from vegetation through transpiration (T) can be different than that of evapotranspiration (ET) from the ecosystem, it is hypothesized that ESI or ESR may not be sufficiently representative of the vegetation evaporative stress. Using eddy covariance flux tower data of 518 site years, distributed across 49-sites and 9 land covers globally, our findings reveal underestimation of vegetation evaporative stress by ESI during periods of high vapor pressure deficit (VPD) and overestimation during dry, low-VPD periods. The results highlight the need to improve representativeness of ESI for monitoring vegetation evaporative stress. Notably, this may entail accurate estimation of ecosystem T in systems lacking in-situ data, a challenge that warrants further attention.

Key Points

- Ecosystem-level Evaporative Stress Index (ESI) tends to underestimate the vegetation evaporative stress, especially during high vapor pressure deficit periods.
- Discrepancies between ESI and ESI_v are larger during non-growing seasons and small during growing seasons.
- The variation of ESI between dry and wet periods can be markedly different from that of ESI_v.

1. Introduction

Global climate change in the recent decades has intensified both the frequency and intensity of the extreme drought events across several parts of the world (Perkins et al., 2012; Seneviratne, 2022). Prolonged dry spells give rise to increase in atmospheric water demand that further depletes the soil moisture availability for plant's photosynthetic activity, thus inducing plant stress. This can affect the overall plant health from germination to maturity (Alamri et al., 2020; Rai et al., 2021; Reich et al., 2018; Yang et al., 2019) and may also eventually trigger plant mortality (Blackman et al., 2016; Liu et al., 2017; McDowell et al., 2008; Niu et al., 2014). Dry spells have been known to affect swaths of forests and cropped areas (Littell et al., 2016; Ray et al., 2018) with significant consequences on water, nutrient, and energy cycling (Adams and Warren Jr, 2005; Bond et al., 2008; Meng et al., 2014; Miralles et al., 2019; Ronda et al., 2001; Schumacher et al., 2022; Van Dijk et al., 2013). Given that these impacts often cause debilitating economic losses (Zamuda et al., 2013), it becomes imperative to establish reliable indicators for vegetation stress (Bachmair et al., 2018; Brown et al., 2008; Gouveia et al., 2017). These indicators could play a crucial role in tracking the level of stress that plants may experience due to soil moisture limitation and increasing atmospheric aridity. Moreover, these indicators can be used to establish an early warning system that enables users to assess and monitor the plant's health to make well-informed management choices. In other words, these indices may also help support efforts to mitigate drought-related challenges and enhance climate adaptation measures.

One of the most widely used ecosystem-level stress indices is the Evaporative Stress Index (ESI) or the Evaporative Stress Ratio (ESR) (Anderson et al., 2011, 2007; Otkin et al., 2013). These indices are defined as the ratio of actual ET to potential evapotranspiration (PET), i.e., ESI=ET/PET. Both indices are used interchangeably, although the

* Corresponding author.
E-mail address: mkumar4@eng.ua.edu (M. Kumar).

https://doi.org/10.1016/j.agrformet.2024.110195
Received 20 November 2023; Received in revised form 5 August 2024; Accepted 12 August 2024
Available online 19 August 2024

term ESI is generally used when it is derived based on remote sensing data, while ESR is used when both ET and PET are obtained using observed or reanalysis meteorological data. These indices have been used extensively to infer flash drought stress (Christian et al., 2019; Lorenz et al., 2021; Zeng et al., 2023) and track agricultural and forest droughts (Anderson et al., 2016a, 2016b; Gazol et al., 2017; Nguyen et al., 2019; Vicente-Serrano et al., 2020; Yang et al., 2021). In this study, for the sake of brevity, we will only use ESI to refer to ecosystem-level evaporative stress. The ensuing analysis, however, is valid for both ESI and ESR.

The evaluation of ecosystem-level ESI uses ET, which is composed of two primary components: 1. abiotic component (E) (direct evaporation from soil and other open surfaces) and 2. biotic component (T) (plant transpiration). Relative contributions of E and T to ET vary in space and time, in part due to the varied environmental controls on E and T (Unkovich et al., 2018). For instance, in addition to the meteorological, soil, and plant morphometric properties that influence E, T is also majorly influenced by plant physiology (Liu et al., 2020; Stoy et al., 2019; Sun et al., 2019). Given that T and E respond to hydrometeorological conditions differently, it is possible that the ESI, which uses ET, may not accurately represent the true evaporative stress experienced by vegetation, which instead is a function of T. Additionally, to capture the vegetation evaporative stress or the constraint on potential water loss by plants due to hydroclimatic-stress driven restriction of stomatal conductance, the potential water loss should ideally be evaluated using place-specific vegetation properties instead of a vegetation-agnostic potential loss, which is often how the ESI has been evaluated in previous literature. While this evaluation is certainly challenging over large areas, at sites where evapotranspiration is observed, there is an opportunity to derive the vegetation properties and then assess the representativeness of ecosystem-level evaporative stress indices for capturing evaporative stress of vegetation.

In this study, we investigate whether the dynamics of ESI is sufficiently representative of evaporative stress in vegetation (ESI_v, henceforth). We specifically analyze the extent of differences between ESI and ESI_v under different regimes of soil moisture (SM) and vapor pressure deficit (VPD). We also compare the spatial variation of evaluated stress across sites, which can be useful to identifying locations that experience more/less evaporative stress. To achieve the aforementioned goals, we use eddy covariance flux tower data of 518 site years across 49 sites distributed across 9 land covers globally and model outputs from a physics-based two-source model for evaluating evapotranspiration.

2. Materials and methods

The methodologies for calculating ESI and ESI_v are elaborated below in Sections 2.1 to 2.7. The datasets utilized for these evaluations are described in Section 2.8.

2.1. Calculation of ESI and ESI_v

ESI, which represents evaporative stress index at ecosystem scale, is quantified as the ratio of the total evapotranspiration (ET) to the potential evapotranspiration (PET):

$$ESI = \frac{ET}{PET} \tag{1}$$

Evaporative stress index for vegetation, hereafter referred as ESI_v, can be evaluated as the ratio of the plant transpiration (T) to the plant's potential evapotranspiration (PET_v):

$$ESI_v = \frac{T}{PET_v} \tag{2}$$

Both ESI and ESI_v can have values between 0 (high stress) and 1 (no stress). When ESI (ESI_v) equals 1, it signifies that ET (T) has reached its maximum potential value with soil and stomatal conductance reaching their peak values, unrestricted by hydrometeorological conditions such as limited soil moisture, light, or unfavorable temperature. A reduction in ESI or ESI_v from 1 indicates the presence of various environmental stresses that constraint the evaporation rate below its potential value. Calculation of ET, PET, T, and PET_v are presented in the subsequent subsections.

2.2. Modeling ET and T

In this study, ET is estimated utilizing a dual-source ET model based on Shuttleworth and Wallace (1985), where ET is computed as the sum of soil evaporation (E) and plant transpiration (T) as:

$$\lambda ET = \lambda E + \lambda T = f_s PM_s + f_c PM_c \tag{3a}$$

$$PM_s = \frac{sA + \left(\rho_a C_p (e_s - e_a) - s r_{as}(A - A_s)\right)/(r_{aa} + r_{as})}{s + \gamma(1 + r_{ss}/(r_{aa} + r_{as}))} \tag{3b}$$

$$PM_c = \frac{sA + \left(\rho_a C_p (e_s - e_a) - s r_{ac} A_s\right)/(r_{aa} + r_{ac})}{s + \gamma(1 + r_{sc}/(r_{aa} + r_{ac}))} \tag{3c}$$

In Eqs. (3a-3c), subscripts s and c represent soil and canopy components, respectively. f_s and f_c are the weighting factors for soil and canopy, respectively, which are calculated using Eqs. (3d-3h). PM_s and PM_c represent the soil evaporation flux and transpiration flux, respectively, before weighting, similar to the Penman-Monteith method (Monteith, 1965b) under bare soil conditions and closed canopy conditions, respectively. s $(Pa\ K^{-1})$ is the slope of the saturated vapor pressure curve. A $(W\ m^{-2})$ is the total available energy for sensible and latent heat flux (i.e., $A = R_n - G$, where R_n $(W\ m^{-2})$ is net radiation and G $(W\ m^{-2})$ is the ground heat flux), A_s $(W\ m^{-2})$ is the part of A available to soil, γ $(Pa\ K^{-1})$ is the psychrometric constant, C_p $(J\ kg^{-1}\ K^{-1})$ is the specific heat of dry air at constant pressure, ρ_a $(kg\ m^{-3})$ is the density of the air, VPD (Pa) is the vapor pressure deficit, r_{aa} $(s\ m^{-1})$ is the aerodynamic resistance between the canopy source and a reference height, r_{as} $(s\ m^{-1})$ is the resistance of vapor transfer between the soil surface and the canopy layer, r_{ac} $(s\ m^{-1})$ is the canopy boundary layer resistance, r_{ss} $(s\ m^{-1})$ is the soil surface resistance for vapor transfer (see Section 2.4), and r_{sc} $(s\ m^{-1})$ is the canopy-scale stomatal resistance (see Section 2.5).

Furthermore,

$$f_c = \frac{1}{1 + R_c \cdot R_a/(R_s \cdot (R_c + R_a))} \tag{3d}$$

$$f_s = \frac{1}{1 + R_s \cdot R_a/(R_c \cdot (R_s + R_a))} \tag{3e}$$

$$R_c = (s + \gamma) \cdot r_{ac} + \gamma \cdot r_{sc} \tag{3f}$$

$$R_s = (s + \gamma) \cdot r_{as} + \gamma \cdot r_{ss} \tag{3 g}$$

$$R_a = (s + \gamma) \cdot r_{aa} \tag{3h}$$

Additionally,

$$A = R_n - G \tag{3i}$$

$$A_s = R_{ns} - G \tag{3j}$$

$$R_{ns} = R_n \exp(-k_r \cdot LAI) \tag{3k}$$

where k_r (=0.6) is the canopy extinction coefficient of net radiation, and LAI $[m^2\ m^{-2}]$ is the all-sided leaf area index. R_{ns} $(W\ m^{-2})$ is the net radiation flux available for the soil which is estimated using Beer's law (Ross and Ross, 1981). Subsequent sections describe the calculation of different resistance terms used in the above equations.

2.3. Calculating aerodynamic resistances

Calculation of different aerodynamic resistances follow the method presented in Wei et al. (2017) and is described below. Aerodynamic resistance between the canopy source height and reference level (r_{aa}) is calculated as:

$$r_{aa} = \frac{1}{k \cdot u^*} \log\left(\frac{z_m - d_0}{h_c - d_0}\right) + \frac{h_c}{k_m \cdot K_h}\left(exp\left(k_m \cdot \left(1 - \frac{d_0 + z_0}{h_c}\right)\right) - 1\right) \quad (4a)$$

Aerodynamic resistance between the substrate and canopy source height (r_{as}) is calculated as:

$$r_{as} = \frac{h_c \cdot \exp(k_m)}{k_m \cdot K_h}\left(\exp\left(\frac{-k_m \cdot z_{0s}}{h_c}\right) - \exp\left(-k_m \cdot \left(\frac{d_0 + z_0}{h_c}\right)\right)\right) \quad (4b)$$

In above equations, k (=0.41 [-]) is a Karman's constant, u^* ($m\ s^{-1}$) is friction velocity, z_m (m) is the measurement/reference height, d_0 (m) is the zero-plane displacement height (see Eqn. (4c) below), h_c (m) is the canopy height, k_m ($= 4.5\ m^2 s^{-1}$) is the extinction coefficient of eddy diffusion, K_h ($m^2 s^{-1}$) is the eddy diffusion coefficient at the top of the canopy (see Eqn. (4f) below), z_0 (m) is the roughness length (see Eqn. (4d)), and z_{0s} (=0.01 m) is the effective roughness length.

$$d_0 = 1.1 h_c \cdot \log\left(1 + X^{\frac{1}{4}}\right) \quad (4c)$$

$$z_0 = \begin{cases} z_{0s} + 0.3 h_c \cdot X^{\frac{1}{2}} & 0 < X < 0.2 \\ 0.3 h_c \left(1 - \frac{d_0}{h_c}\right) & 0.2 < X < 1.5 \end{cases} \quad (4d)$$

$$X = C_d \cdot LAI \quad (4e)$$

$$K_h = k \cdot u^* \cdot (h_c - d_0) \quad (4f)$$

The bulk boundary layer resistance of the vegetative elements in the canopy (r_{ac}) is calculated as:

$$r_{ac} = \frac{r_b}{2LAI} \quad (4\ g)$$

where, r_b ($s\ m^{-1}$) is the mean boundary layer resistance per unit area of vegetation and is calculated as:

$$r_b = \frac{\frac{100}{k_m}\left(\frac{d_l}{u_h}\right)}{1 - \exp\left(-\frac{k_m}{2}\right)} \quad (4h)$$

In Eqn. (4e), C_d [-] is the drag coefficient, and in Eqn. (4h), d_l [m] is the characteristic leaf dimension.

2.4. Calculating soil surface resistance

The calculation of soil surface resistance (r_{ss}) is presented in Sellers et al. (1992) where r_{ss} is defined as the function of soil wetness of the top soil layer.

$$r_{ss} = \exp(\alpha - \beta \cdot \theta / \theta_s) \quad (5a)$$

In Eq. (5a), θ ($m^3\ m^{-3}$) is the actual surface soil moisture content, and θ_s ($m^3\ m^{-3}$) is the saturated soil moisture content. θ_s is obtained using the empirical relations provided in Clapp and Hornberger (1978). α and β are the two empirical parameters of Sellers' equation with suggested values of 8.2 and 4.3 for α and β, respectively (Kustas and Norman, 1999). However, choice of these empirical parameters can introduce large uncertainty in the calculation of r_{ss} and thus soil evaporation (E). In this study, we use the following procedure to obtain α and β for each site. First, the ecosystem conductance (G_s) is obtained by inverting the Penman-Monteith equation using flux tower data as:

$$G_s = \frac{\gamma \cdot G_a \cdot LE}{s \cdot (R_n - G) + \rho_a \cdot C_p \cdot G_a \cdot VPD - (s + \gamma) \cdot LE} \quad (5b)$$

where G_a is the aerodynamic conductance ($m\ s^{-1}$), and LE is the latent heat flux ($W\ m^{-2}$). Rest of the terms in the Eq. (5b) are already defined above. G_a is calculated following Lin et al. (2018) including corrections factors for stability. Ideal gas law is used to convert G_s from $m\ s^{-1}$ to $mol\ m^{-2}\ s^{-1}$. Ecosystem conductance calculated above is the sum of soil conductance (G_{ss}), canopy conductance (G_{sc}), and conductance of intercepted water. As this study does not include periods during rainfall (see Section 2.8 below for more information on data quality control), G_s is only the sum of G_{ss} and G_{sc}, i.e.,

$$G_s = G_{ss} + G_{sc} \quad (5c)$$

To obtain G_{ss} from G_s, here we use a generalized ecosystem conductance model described in Li et al. (2019):

$$G_s = G_{ss} + G_1 \cdot \frac{GPP}{VPD^m} \quad (5d)$$

Next, we sort the data of G_s, GPP, and VPD into different categories (0–15th, 15–30th, 30–50th, 50–70th, 70–85th, and 85–100th percentiles) of soil moisture at each site. A non-linear regression is fitted to Eq. (5d) to obtain regression parameters (G_{ss}, G_1, and m) for each soil moisture category at each site (see Li et al. (2019) for more details.). The values of G_{ss} obtained above are then used to obtain α and β in Eq. (5a) (note that $r_{ss} = 1/G_{ss}$). For the few sites where either α or β is negative, we use standard values of 8.2 and 4.3 respectively, following previous studies (Kustas and Norman, 1999; Wei et al., 2018).

2.5. Calculating canopy conductance

To calculate ET and/or T, one critical variable that still needs to be computed is g_{sc}. To compute g_{sc}, here we use a plant physiological approach based on (Ronda et al., 2001) as described below.

At the leaf scale, the CO_2 stomatal conductance can be characterized using a photosynthesis-stomatal conductance model, which is defined as (Ronda et al., 2001):

$$g_{sc}^l = g_{sc}^{min} + \frac{a_1 \cdot A_g}{(C_s - \Gamma)\left(1 + \frac{D_s}{D_0}\right)} \quad (6a)$$

where g_{sc}^{min} ($mol\ m^{-2} s^{-1}$) is the cuticular conductance, a_1 is an empirical parameter (= 9.1 for C3 plants, and 6.6 for C4 plants), A_g ($\mu mol\ m^{-2}\ s^{-1}$) is the gross assimilation rate (see Eq. (6b)), C_s (ppm) is the CO_2 concentration at leaf level, Γ ($\mu mol\ mol^{-1}$) is CO_2 compensation point that is a function of the canopy temperature, D_s (kPa) is the vapor pressure deficit at leaf level, and D_o (which represents the value of D_s at which all stomata are closed) is a tunable parameter (see Section 2.7 for the estimation of different parameters).

In this study, A_g is computed as a function of photosynthetically active radiation (PAR), canopy temperature (T_c), and the intercellular CO_2 concentration (C_i) as:

$$A_g = (A_m + R_d)\left[1 - e^{-\frac{\alpha PAR}{A_m + R_d}}\right] \quad (6b)$$

Here, A_m ($\mu mol\ m^{-2}\ s^{-1}$) is the net primary productivity which is computed as:

$$A_m = A_{m,max}\left(1 - e^{-\frac{g_m(C_i - \Gamma)}{A_{m_{max}}}}\right) \quad (6c)$$

and R_d ($\mu mol\ m^{-2}\ s^{-1}$) is the dark respiration which is computed as:

$$R_d = 0.11A_m \tag{6d}$$

where α is the light use efficiency which is calculated as:

$$\alpha = \alpha_0 \frac{C_s - \Gamma}{C_s + 2\Gamma} \tag{6e}$$

with α_0 = 0.017 (mg/J) for C3 plants and α_0= 0.014 (mg/J) for C4 plants. $A_{m,max}$ is the maximal primary productivity under high light and high CO_2 concentrations, and g_m is the mesophyll conductance for CO_2, which are functions of T_c (Ronda et al., 2001). T_c is solved iteratively by combining a photosynthesis model (Eq. (6b)) with stomatal conductance model (Eq. (6a)) along with the T fluxes predicted by S-W model as detailed elsewhere in Wei et al. (2018). For detailed calculation of g_m, $A_{m,max}$, and Γ, readers are encouraged to refer to Ronda et al. (2001).

Furthermore, we also consider the effects of water stress on A_g and g_{sc} by applying a soil-moisture dependent function to A_g as:

$$A_g = A_g^* f(\theta) \tag{6f}$$

where A_g^* is the unstressed A_g rate, and $f(\theta)$ is computed as:

$$f(\theta) = 2\beta(\theta) - \beta^2(\theta) \tag{6 g}$$

with

$$\beta(\theta) = \max\left(0, \min\left(1, \frac{\theta - \theta_{wp}}{\theta_s - \theta_{wp}}\right)\right) \tag{6h}$$

where θ $(m^3\ m^{-3})$, θ_{wp} $(m^3\ m^{-3})$, and θ_s $(m^3\ m^{-3})$ are actual soil moisture content, soil moisture content at permanent wilting point, and soil moisture content at saturation, respectively. θ_{wp} and θ_s are obtained using the empirical relations provided elsewhere (Clapp and Hornberger, 1978; Saxton et al., 1986) based on basic soil properties (i.e., sand-silt-clay fractions) (Dai et al., 2019).

Leaf scale g_{sc} (g_{sc}^l) is upscaled to canopy scale g_{sc} following Ronda et al. (2001). Finally, r_{sc} ($s\ m^{-1}$) is calculated as:

$$r_{sc} = \frac{1}{1.6 g_{sc}} \tag{6i}$$

where 1.6 is used to account for the diffusion of water vapor and carbon dioxide by the same stomata.

2.6. Calculating potential evapotranspiration

Many different methods have been proposed for the calculation of PET (Hargreaves and Samani, 1985; Monteith, 1965a; Oudin et al., 2005; Penman, 1948; Priestley and Taylor, 1972; Thornthwaite, 1948). In this study, we use three different methods for obtaining potential evapotranspiration as described below. The use of multiple methods allows assessment of the influence of PET formula on ESI estimation. It is to be noted that only the S-W model is used to obtain PET of plant (i.e., PET_v) as described below. S-W model and two other methods (i.e., Penman method and Priestley-Taylor method) are used to obtain PET of the ecosystem.

2.6.1. S-W model-based potential evapotranspiration

To obtain PET and PET_v from the S-W model (see Eqn. 3), g_{sc} is set to unstressed conditions of soil moisture, temperature, radiation, VPD, and CO_2. In other words, the predicted ET (T) from S-W model is equivalent to PET (PET_v) when the model is run under the aforementioned unstressed conditions. Obtaining PET from this approach ensures that PET calculation uses the site-specific parameters of the plants.

2.6.2. Potential evapotranspiration from penman equation

Second approach to obtain PET is based on Penman (1948). Here, PET ($mm\ day^{-1}$) is computed as:

$$PET = \frac{\Delta(R_n - G) + \gamma \cdot 2.6 \cdot (1 + 0.536u_2) \cdot (e_s - e_a)}{\lambda(\Delta + \gamma)} \tag{7}$$

where Δ ($Pa\ K^{-1}$) is the slope of the saturation vapor pressure curve, γ $(Pa\ K^{-1})$ is the psychrometric constant, R_n ($MJ\ m^{-2} day^{-1}$) is the net radiation, G ($MJ\ m^{-2} day^{-1}$) is the ground heat flux, u_2 is the wind speed at 2 m height, e_s (kPa) is the saturation vapor pressure, e_a (kPa) is actual vapor pressure of the near surface atmosphere, and λ ($MJ\ kg^{-1}$) is the latent heat of vaporization.

2.6.3. Potential evapotranspiration from priestley-taylor equation

Third approach to obtain PET is based on the Priestley-Taylor equation (Priestley and Taylor, 1972). Here, PET ($mm\ day^{-1}$) is computed as:

$$PET = \alpha_{PT} \frac{\Delta(R_n - G)}{\lambda(\Delta + \gamma)} \tag{8}$$

where α_{PT} is an empirical constant (=1.26 in this study). All other terms have the same meaning as described for Eqn. (7).

2.7. Estimation of model parameters for ET prediction

The S-W model is trained for each site individually to ensure that model performs optimally for each site. Notably, combining S-W model with g_{sc} leaves six unknown parameters, viz. D_0, k_m, Z_{0s}, d_l, C_d, and g_{sc}^{min}. These parameters are optimized using the Shuffled Complex Evolution approach (Duan et al., 1993) while ensuring that the mean square errors between observed and modeled ET fluxes are minimized.

2.8. Datasets and site properties

The S-W model is run at 49 flux tower sites (Fig. 1) using the PLUMBER2 dataset (Ukkola et al., 2022). Sites are chosen to ensure that soil moisture data are available, and all other required variables are available for at least over 5 years (see Table S1). These flux sites are located in 9 different landcover types including closed shrublands (CSH, $N = 1$), croplands (CRO, $N = 9$), deciduous broadleaf forests (DBF, $N = 5$), evergreen broadleaf forests (EBF, $N = 2$), evergreen needleleaf forests (ENF, $N = 15$), grasslands (GRA, $N = 9$), mixed forests (MF, $N = 2$), savannas (SAV, $N = 3$), and woody savannas (WSA, $N = 3$), where N represents the number of flux sites in each landcover type. PLUMBER2 dataset has been compiled from the FLUXNET2015, OzFlux, and La Thuile collections, after quality control and gap-filling to make it suitable for land surface modeling. The sampling frequency of data is either half-hourly (for 44 sites) or hourly (for 5 sites) across the sites. The measurements of LE and H are corrected for energy balance closure using a Bowen ratio method (Barr et al., 2006; Xu et al., 2013) when the energy imbalance, i.e., $(LE+H)/(R_n\text{-}G)$ is less than 0.8. Reference heights of flux measurement and mean canopy heights are obtained from site-specific metadata information. PLUMBER2 dataset also provides leaf area index (LAI) for each site derived from MODIS (Moderate Resolution Imaging Spectroradiometer) product (MCD15A2H.006) with a temporal resolution same as the flux measurements. Basic soil properties including sand-silt-clay fractions are obtained from the soil map used in Noah-LSM (Dai et al., 2019).

To validate the transpiration estimates from the S-W model, sap flow data from SAPFLUXNET database (Poyatos et al., 2020) is obtained for the sites used in this study (Table S3). The SAPFLUXNET datasets contain sub-daily sap flow rates that are scaled to the stand level using site-specific procedures, as detailed in the dataset metadata (Poyatos et al., 2019). To derive stand-level transpiration (T), we first aggregate the sub-daily data to obtain daily sap flow values per tree (kg/day). Subsequently, we apply a correction factor of 1.405 to the sap flow values based on an extensive analysis of sap flow calibrations (Bright

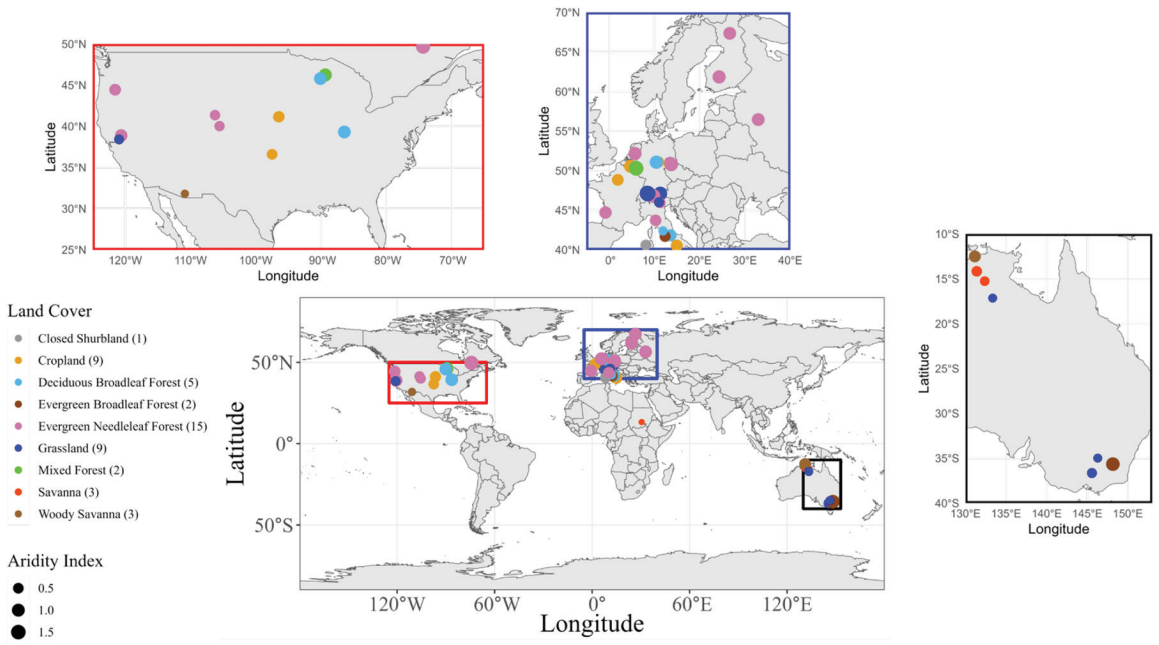

Fig. 1. Spatial distribution of eddy covariance sites (shown as colored circular dots) utilized in this study. Colors of the dots indicate the land cover types, while their size represents the aridity index of each site. A smaller aridity index (i.e., smaller dot size) indicates a drier site and a larger aridity index (i.e., larger point size) indicates a wetter site. Number in the parenthesis besides each land cover in the legend indicate the number of sites in that land cover type.

et al., 2022; Flo et al., 2019). Next, we normalize the sap flow per unit basal area for each tree and calculate the average values for each species present in the datasets. Notably, the species included in the sap flow measurements accounted for over 90 % of the stand basal area (Table S3) at the sites. The species-specific sap flow per basal area is then multiplied by the basal area of each species in the stand, and the resulting values are summed across all species to obtain stand-level transpiration (mm/day). All tree and stand-level variables required for this upscaling process are extracted from the corresponding dataset metadata (Poyatos et al., 2019).

We next conduct simulations using the S-W model, as well as the Penman and Priestley-Taylor methods, at the same temporal resolution as the original dataset, which is half-hourly for most of the sites. This generates half-hourly estimates of ET, T, PET, and PET_v. For sites where data are available only at an hourly scale (5 out of 49 sites), we obtain hourly estimates of these fluxes instead. Subsequently, we aggregate these fluxes to derive daily estimates of ET, T, PET, and PET_v, and ultimately, ESI and ESI_v. It is important to note that during this process, some calculated ESI or ESI_v values are deemed unrealistic, such as when ESI falls below 0 or exceeds 1. These occurrences may be attributed to uncertainties in input data or model performance. To ensure a fair comparison between these indices, we exclude such instances from our analysis both for ESI and ESI_v. We quantify the differences in the indices for the full length of record as well as for specific regimes of soil moisture and VPD. These regimes are delineated using cutoffs at the 75th and 25th percentiles, to identify high and low extremes, respectively, of the variable under consideration at each site.

3. Results and discussion

3.1. Performance of the S-W model across different flux sites

We first compare the performance of S-W model for predicting ET at all selected sites. In general, the model successfully predicts the ET for most of the sites in different land cover types (Fig. 2). The overall model performance across all the sites is shown in Fig. S1. The coefficient of

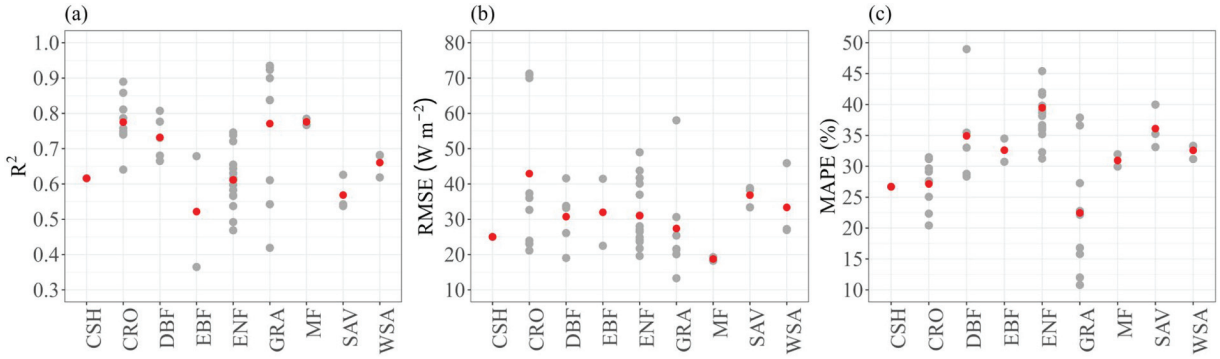

Fig. 2. Performance statistics of the S-W model for prediction of evapotranspiration (ET) at the temporal resolution of flux measurements (i.e., 30 min or 1 h). R^2, RMSE, and MAPE (shown using gray dots for the considered eddy covariance sites) represent the coefficient of determination, root mean square error, and mean absolute percentage error, respectively, between the observed ET fluxes and predicted ET fluxes. Red dot represents the mean values. Performances are shown for sites belonging to different biomes (X-axis). CSH: Closed Shrublands, CRO: Croplands, DBF: Deciduous Broadleaf Forests, EBF: Evergreen Broadleaf Forests, ENF: Evergreen Needleleaf Forests, GRA: Grasslands, MF: Mixed Forests, SAV: Savannas, WSA: Woody Savannas.

determination (R^2) varies between 0.36 to 0.94 with an average value of 0.69. The Root Mean Square Error (RMSE) varies between 13.3 $W\ m^{-2}$ to 71.3 $W\ m^{-2}$ with an average value of 32.4 $W\ m^{-2}$. The Mean Absolute Percentage Error (MAPE) varies between 10.8 % to 63.7 % with an average value of 32.1 %. The S-W model performs the best in cropland, mixed forest, and grassland settings with an average R^2 of 0.78, 0.78, and 0.77, respectively. Fig. S2 (see supplementary document) shows the comparison of modeled ET with observed ET for all the time periods as well as during different regimes of SM and VPD across all the sites. More details on the model performance for each site under different regimes of SM and VPD can be found in Table S2 in the supplementary document. The model shows satisfactory performance ($R^2 \geq 0.5$) in all the scenarios including the extreme regimes (Fig. S2). When compared to independent sap flow measurements at the only three sites out of 49 with such data available, transpiration estimates from the S-W model show a high correlation (0.76–0.87) to sap flow-based T estimates demonstrating effectiveness of the S-W model for both ET predictions and T predictions (Fig. S3).

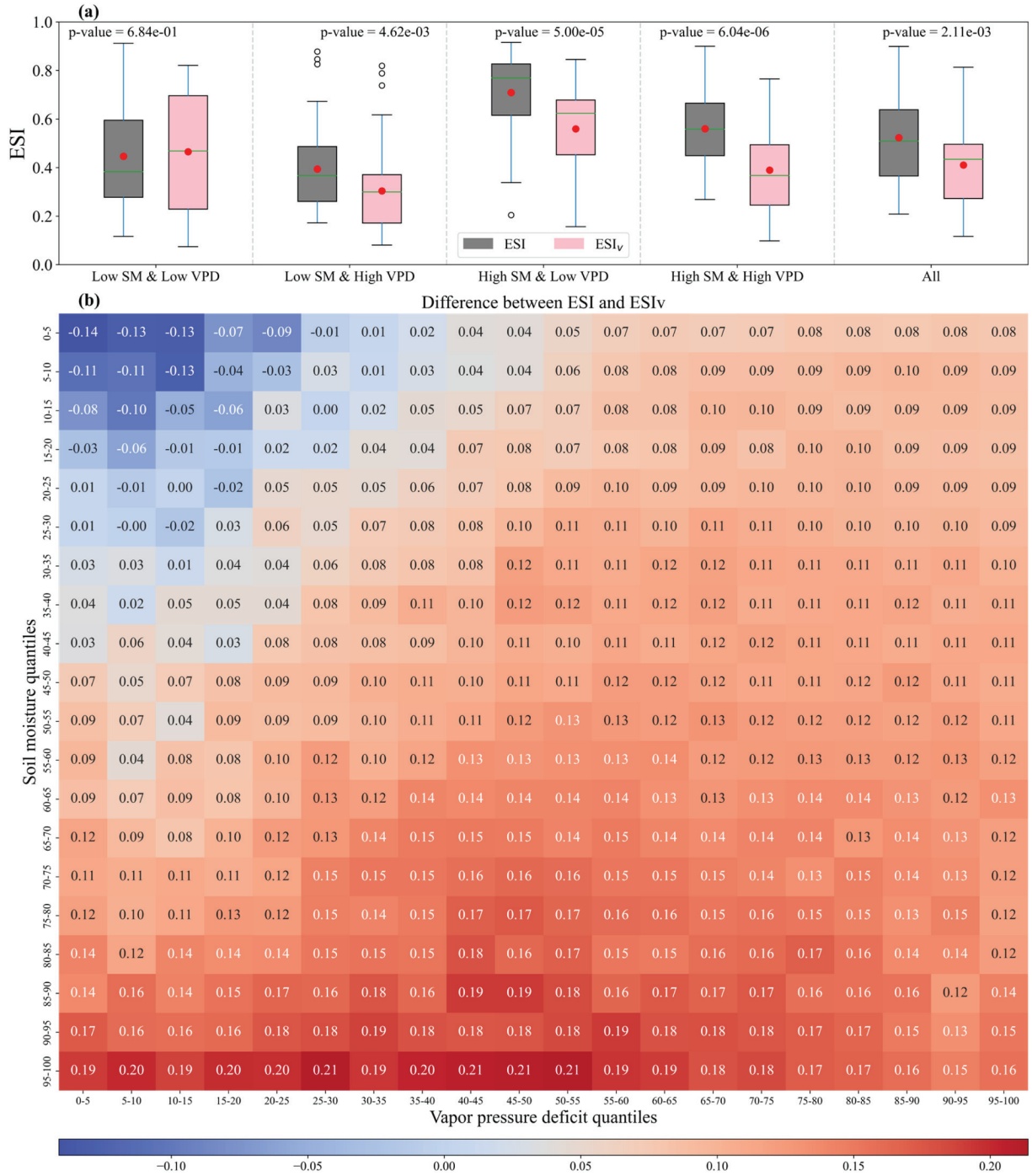

Fig. 3. Comparison of traditional Evaporative Stress Index (ESI) and ESI for vegetation (ESI_v) across all the sites: Panel (a) shows the variation of mean ESI and ESI_v during extremes of soil moisture (SM) and vapor pressure deficit (VPD), as well as across all time periods. Panel (b) illustrates the variations in the difference between ESI and ESI_v across a range of SM and VPD. In Panel (a), red dots represent the mean values. The label 'All' indicates aggregation across all time periods. The p-value displayed in each box of panel (a) indicates the significance of the difference between ESI and ESI_v, as determined by the Mann-Whitney U test. Note that here PET is calculated using the Shuttleworth-Wallace model. For additional insights based on alternative PET methods, refer to supplementary Figures S4-S5.

3.2. Comparison between ESI and ESI_v vis-à-vis moisture deficit regimes of the soil and atmosphere

We compare the estimates of ESI with that of ESI_v at each site for all periods, and also under different regimes of soil moisture (SM) and vapor pressure deficit (VPD). Fig. 3 illustrates the mean ESI and mean ESI_v at each site under different regimes of SM and VPD. Here, "high" and "low" periods within a specific regime is based on "larger than 75th percentile" and "smaller than 25th percentile" thresholds of the respective variable (i.e., SM or VPD) at each site as described in Section 2.8. It is evident from Fig. 3 that ESI is consistently higher (i.e., the evaporative stress is lower) than ESI_v under high VPD periods regardless of whether SM levels fall within high or low regimes. Notably, ESI and ESI_v are significantly different with p-value < 0.05 based on the Mann-Whitney U test during high VPD periods. This is true irrespective of the PET method used (Figures S4-S5). The results indicate that plants are in more stress than predicted by the ESI during the periods of low SM and high VPD when vegetation is expected to experience higher stresses. These results are further supported by Fig. S6 in the supplementary document where we can see that the difference of ESI and ESI_v is always positive for high VPD periods irrespective of the PET method used. In contrast, during low VPD and low SM periods, ESI is lower than ESI_v, irrespective of the method used for evaluating PET. It means that plants are in less stress than indicated by the ESI during low SM and low VPD periods. Notably, during low SM and low VPD periods, ESI and ESI_v are not significantly different (p-value > 0.05) when considering PET from the S-W model. Overall, the conclusions drawn from comparisons between ESI and ESI_v for different VPD and SM regimes are observed to be valid for other quantiles of SM and VPD as well (see Fig. 3b and Figures S4b-5b). When all the time periods are considered, ESI is overall higher than ESI_v, thus indicating that ESI underestimates vegetation stress (Fig. 3, Fig. S4-S6). It is worth mentioning that the performance of the S-W model for predicting ET may be inadequate for certain sites. To ensure that such sites do not unduly influence the conclusions of this study regarding the significant difference between ESI and ESI_v during periods of high VPD, we conduct further investigations. Even after excluding sites with suboptimal performance, our analysis reveals a consistent pattern in our findings, as illustrated in Figure S7.

3.3. Temporal dynamics of ESI and ESI_v during wet and dry years

Next, we investigate the temporal dynamics of ESI and ESI_v during wet and dry years to understand the behavior of these indices within, and between a dry and a wet year. For this, we select two sites (US-Ne3 and US-MMS) (see Table S1 in the supplementary document) as example sites for analysis. Site US-Ne3 is a rainfed cropping site with a maize-soybean rotation cropping system (Suyker and Verma, 2010). At this site, we identify the year 2012 as the dry year with a total yearly rainfall of about 428 mm, and the year 2008 as the wet year with a total yearly rainfall of about 1000 mm (see Fig. S8 in the supplementary document). Site US-MMS at the Morgan-Monroe State Forest is a deciduous broad-leaf forest characterized by an average canopy height of ~27 m and stand age of ~80–90 years (Brzostek et al., 2014). At site US-MMS also, we identify the year 2012 as the dry year with a total yearly rainfall of about 780 mm, and the year 2008 as the wet year with a total yearly rainfall of about 1478 mm (see Fig. S8 in the supplementary document).

Plant stress is expected to increase with the dryness of the atmosphere and the ground. This is evident in both ESI and ESI_v, which are

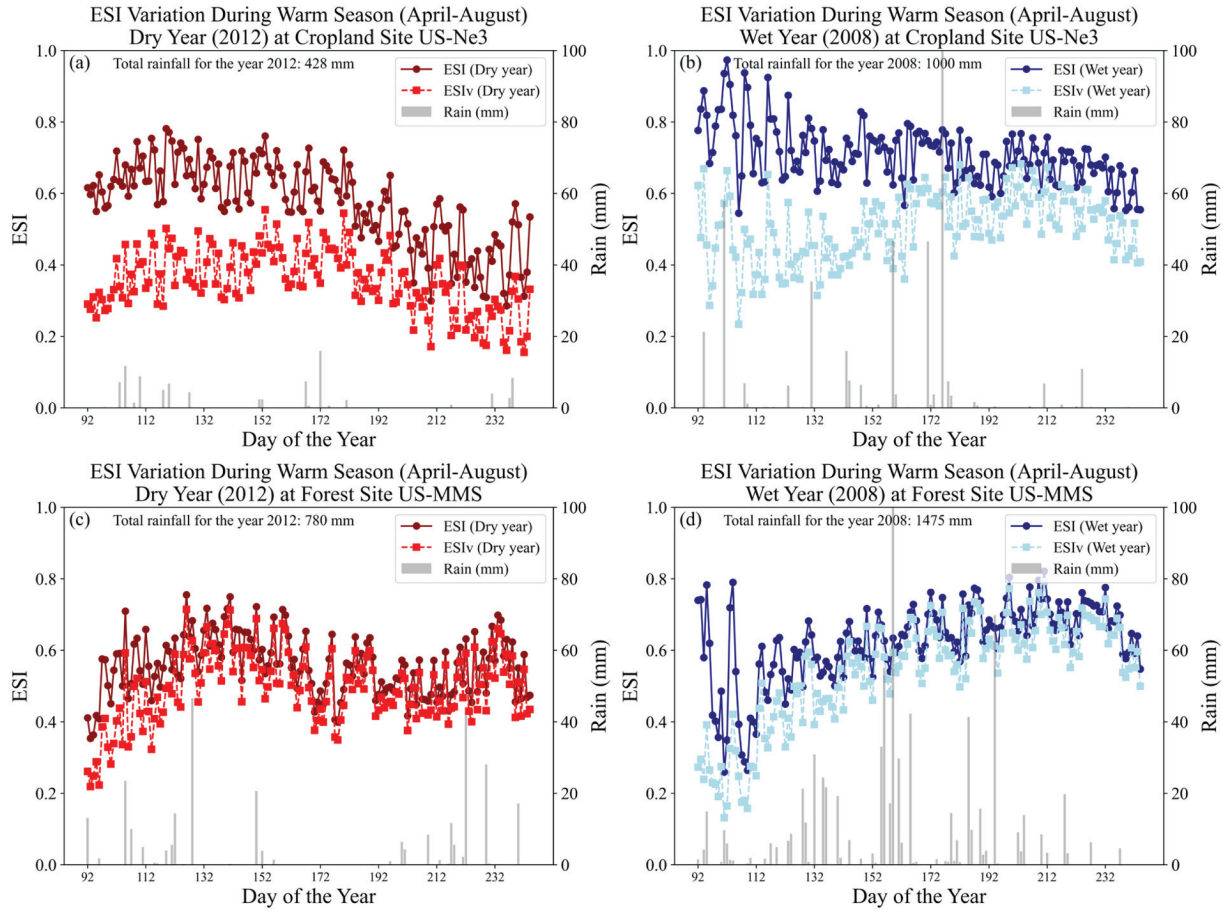

Fig. 4. Daily variation of ESI and ESI_v during the warm season (April-August) at a cropping site US-Ne3 (first row) and a forest site US-MMS (second row) during a dry year (first column) and a wet year (second column). The bars in each panel show the daily rainfall values.

lower during the dry years and higher during the wet years (Fig. 4). Notably, ESI_v is generally smaller than ESI during both years within the two land covers. Interestingly, a decrease in ESI_v due to dryness is much larger than the decrease in ESI at the cropland site. For example, at the site US-Ne3, the reduction in ESI (ESI_v) from wet year to dry year is ~19 % (~29 %). This reduction is about ~8 % for both ESI and ESI_v at the forested site. These results indicate that assessments regarding the fractional increase of evaporative stress experienced by vegetation during dryer periods may get biased if evaluated based on ESI. Notably, while the intra-seasonal variation of ESI and ESI_v are similar during dry years, for wet years, the variation of the two variables shows contrasts. For example, at the selected crop site (US-Ne3) during the wet year, ESI shows an overall decreasing trend while ESI_v does not. Overall, the difference between ESI and ESI_v is larger during the early growing period (see Text S1 for the identification of growing seasons), and it reduces later in the growing season for both dry and wet years. This is likely due to increased influence of transpiration on total evapotranspiration later in the growing season. Difference between ESI and ESI_v is lower at the forested site and larger at the cropland site. This can again be attributed to higher transpiration contribution to ET at the forest site. For example, mean T:ET for US-MMS (mean LAI=2.52) is 0.73, which is higher than at site US-Ne3 (mean T/ET=0.58). In fact, comparison of ESI and ESI_v across all sites reveals that site-averaged difference between the two indices increases for sites with higher E/ET ratio (with E being soil evaporation) (Fig. S9), or smaller overall LAI. Larger difference in ESI and ESI_v or high E/ET are largely governed by T/ET rather than PET_v/PET (Fig. S9). Furthermore, it is found that the difference between ESI and ESI_v is larger during non-growing season than that of growing season (Figures S12-S16). Additionally, the difference between ESI and ESI_v increases with the dryness of the site (Figure S16). Based on these findings, it can be inferred that ESI does not accurately capture the vegetation evaporative stress, especially in settings and periods with greater dryness or a smaller contribution of transpiration to total ET.

3.4. Spatial rank correlation between ESI and ESI_v

Spatial variability of ESI and ESI_v is compared at different temporal scales. Notably, ESI_v between any two sites can be different even if they experience identical hydrometeorological conditions depending on the differences in the plant functional types (PFTs) and the corresponding stomatal kinetics between the sites. Of course the sites with identical PFTs but different meterological forcings are expected to have different vegetation stress as well. One of the goals of this study is to assess whether the relative order of vegetation evaporative stress magnitude, as captured by ESI_v, is representatively captured by ESI. A poor correlation would indicate that ESI maps, which inherently capture the relative distribution of evaporative stress over the area of interest, may not representatively reflect the distribution of plant stress. To assess this, we calculate the spatial correlation between average ESI and ESI_v at daily, weekly, or monthly timescales across all the flux sites. For example, to calculate spatial correlation at daily temporal scale, we first calculate the multiyear mean of daily ESI and ESI_v for all the sites. Then, we calculate the spatial rank correlation of ESI and ESI_v for a given day of the year (say day 145). Similar calculations are performed at weekly and monthly time scales as well. Fig. 5 shows the spatial rank correlation between ESI and ESI_v at three time scales (daily, weekly, and monthly). Results indicate that ESI and ESI_v have high (> 0.8) spatial correlation in space during growing periods (Apr.-Sep.). This covariation becomes poorer during non-growing periods (Oct-Mar). This is overall consistent across all the three PET methods chosen in this study (Figures S17).

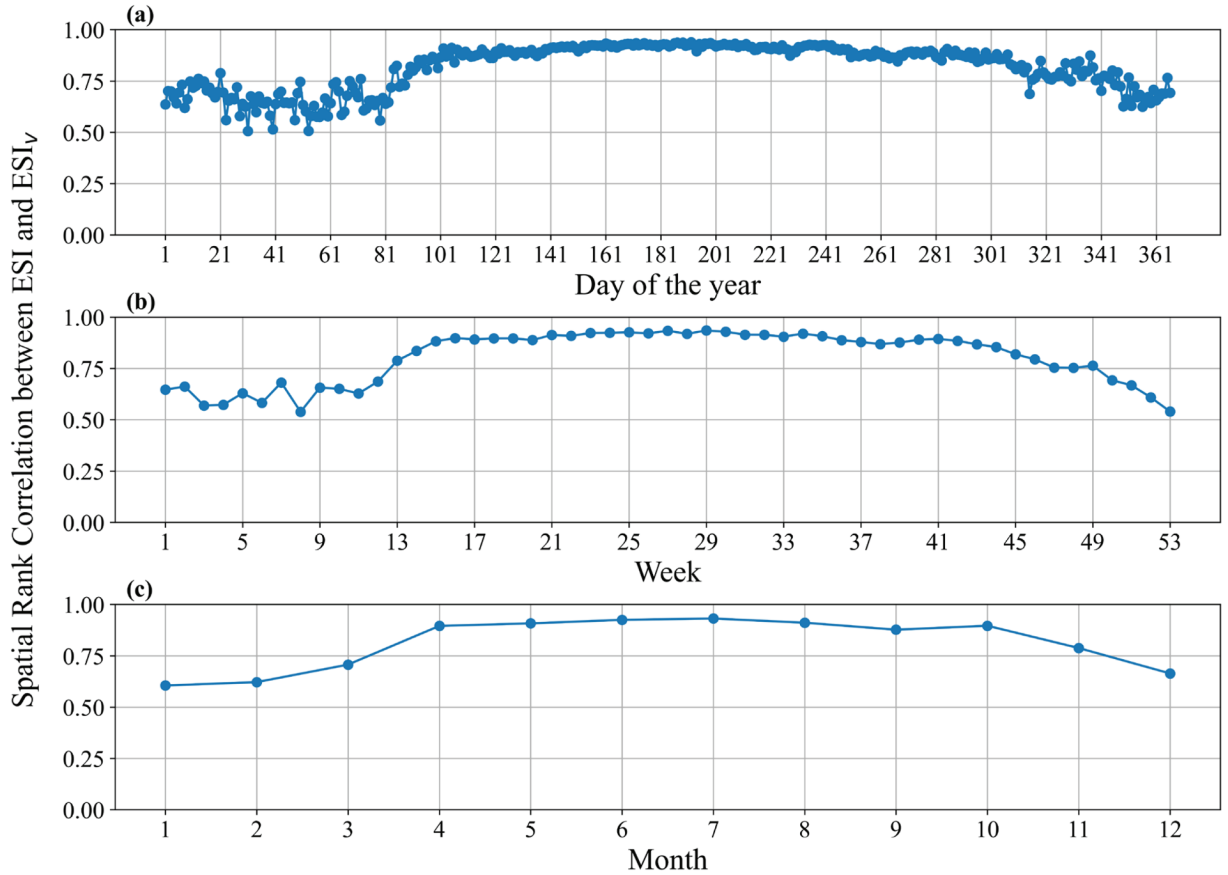

Fig 5. Spatial rank correlation between ESI and ESI_v at different temporal scales, daily (a), weekly (b), and monthly (c). Here the results are based on PET calculation from the Shuttleworth-Wallace model. For additional insights based on alternative PET methods, refer to supplementary Figure S17.

Lower correlation during non-growing season can be attributed to lower stress during this period, which results in milder spatial contrasts across sites. An additional reason for this is the larger difference between ESI and ESI_v during the non-growing season (Figures S12-S16), when contribution of E to ET is relatively large. Spatial correlation is weaker in case of Priestley-Taylor PET method. This can be partially attributed to the fact that Priestley-Taylor PET method does not use any information regarding the plant properties, but the other two methods use this information in the calculation of PET, which in turn enhances the spatial contrasts.

4. Conclusions and synthesis

This study attempted to answer one crucial question: does evaporative stress index (ESI), which is often used to track vegetation health status, and agricultural and forest droughts, representatively capture the evaporative stress that the vegetation actually experiences, i.e., the ESI_v? ESI is usually calculated as the ratio of total water loss from the ecosystem (or total evapotranspiration (ET)) over the potential water demand (or potential evapotranspiration (PET)). However, as it is the transpiration flux (T) rather than the total ET that represents the constrained evaporative response of vegetation due to hydroclimatic stress, there is a likelihood of discrepancy between ESI and ESI_v. This is especially expected as the dynamics of T and E with time are usually different (Gu et al., 2018; Kool et al., 2014; Nelson et al., 2020; Raghav et al., 2022; Talsma et al., 2018; Wagle et al., 2023; Zhou et al., 2016), and the contribution of E to ET can be significant (Wei et al., 2017).

To assess whether the ESI index is limited in capturing the spatio-temporal variations in evaporative stress, we first implemented a two-source physical evapotranspiration model (Shuttleworth-Wallace or S-W) at 49 sites located in 9 different biomes across the globe. After obtaining the model parameters that ensured efffectiveness of S-W model at reproducng ET and T observations, we calculated the ESI (=ET/PET) and ESI_v (ESI_v=T/PET_v). Following the computaion of ESI and ESI_v at daily time scale for each site, we then performed spatio-temporal comparisons between ESI and ESI_v.

The temporal dynamics of ESI and ESI_v under different regimes of soil mositure and atmospheric aridity were first compared. Our results showed that conventional ESI underestimates the vegetation evaporative stress, especially during the periods of high atmospheric water demand. Furthermore, ESI overestimates the plant stress during the period of low SM and low VPD which suggests that plants are actually in less stress during these periods than as indicated by the ESI metric. As these periods are more likely existent during the winter time, it could be crucial for tracking plant stress and its consequences on winter crops. Aforementioned results were consistent irrespective of the selection of PET method. We also compared the response of ESI and ESI_v for dry and wet periods. Our results showed that both ESI and ESI_v significantly reduce during the dry year. However, reduction in ESI_v is much larger than the reduction in ESI, especially for crops. It indicates that because of drynesss, the increase of plant stress is significantly greater than what is depicted by ESI, which indicates a lesser degree of stress. Furthermore, seasonal variation of ESI and ESI_v were found to be very different.

We then analyzed the spatial dynamics of ESI and ESI_v at different temporal scales. Our results showed that the covariation of ESI and ESI_v was strong spatially during the growing periods. But, this relationship becomes poor during non-growing periods. Generally, growing periods are the crucial periods when tracking the plant is needed (e.g., for agricultural or forest drought monitoring). A strong spatial correlation between ESI and ESI_v during the growing periods shows the effectiveness of current ESI for spatial mapping of areas with higher/lower drought stress. In other words, though ESI underpredicts the plant stress, it can still be used to identify locations with relatively higher or lower stress during the growing season.

The findings of this study lay a crucial foundation for the drought research community, providing valuable insights into the behavior of these indices under varying environmental conditions. This is especially important for understanding and predicting flash drought occurrences. Notably, flash drought identification and assessment are often dependent on drought conditions when evaporative stress indices fall below a defined percentile of their statistical distribution (Christian et al., 2021, 2019; Hobbins et al., 2016; Otkin et al., 2014). Limited length of data at the eddy-covariance sites pose challenge in assessment of such distributions for ESI_v for a given period. Further studies wherein both ESI and ESI_v can be extended for long periods may allow quantitative assessment of the differences in flash drought estimation due to differences in ESI and ESI_v estimates. Overall, the results from this study underscore the need to improve the representativeness of currently used evaporative stress index to monitor the evaporative vegetation stress. Notably, achieving this improvement may require accurate estimation of ecosystem T in systems lacking in-situ data, a task that remains challenging (Stoy et al., 2019). From ease of evaluation standpoint, it is certainly easier and straightforward to obtain ESI as a function of ET and PET, and perhaps this ease explains the wide usage of ESI to track vegetation evaporative stress as well. In contrast, modeling T as well as potential transpiration flux (PET_v), variables needed to obtain ESI_v, is relatively challenging because T is modulated by plant physiological properties related to hydraulics and stomatal kinetics. Deriving these properties over large areas, in a spatially-explicit manner remains challenging, and oftentimes need additional data associated with plant hydraulic status (Liu et al., 2021). Furthermore, validation of modeled T remains challenging as sources of T data, oftentimes obtained from sap flux measurements (Flo et al., 2019; Hernandez-Santana et al., 2015; Mitchell et al., 2009; Poyatos et al., 2016) or from partitioning of ET (Scott and Biederman, 2017; Zahn et al., 2022; Zhou et al., 2016) continue to be beset by uncertainties inherent in these methods. Future studies may focus on deriving remotely sensed data of T and PET_v to extend the utility of ESI_v beyond settings with in-situ data. The goal should include generating the best remote sensing-derived ESI_v after performing validation at eddy-covariance sites. Notably, obtaining remote sensing-derived ESI_v using the methodology outlined in Sections 2.1 to 2.7 would require remotely sensed ET data, soil moisture data (see Equation 6), and various other meteorological variables (e.g., R_n, VPD, wind speed, etc.). Given the resolution mismatch among these data products and the inherent uncertainties in each dataset, a thorough assessment of remotely sensed ESI and ESI_v across multiple data products is necessary.

Data and source code availability statement

All the data sets used in this study are freely available. However, if readers/users face any difficulty to access the data sets, the authors are happy to provide both the data and source code upon reasonable request. PLUMBER2 dataset can be accessed at http://doi.org/10.25914/5fdb0902607e1. The original source code for the model can be found at https://github.com/zhongwangwei/SiLSM_v3. Sap flow data can be obtained at https://zenodo.org/records/2530798. Script used to upscale sap flow estimates to stand-scale transpiration can be found at https://github.com/praghav444/Stand-Scale-Transpiration-Estimation-from-SAPFLUXNET-Database.

CRediT authorship contribution statement

Pushpendra Raghav: Writing – original draft, Validation, Resources, Methodology, Investigation, Formal analysis, Data curation, Conceptualization. **Mukesh Kumar:** Writing – review & editing, Project administration, Methodology, Investigation, Funding acquisition, Formal analysis, Conceptualization.

Declaration of competing interest

The authors declare that they have no known competing financial

interests or personal relationships that could have appeared to influence the work reported in this paper.

Data availability

Data will be made available on request.

Acknowledgement

This work is partially supported by NSF OIA-2019561, NSF OIA-2317819, and NSF EAR-1856054.

Supplementary materials

Supplementary material associated with this article can be found, in the online version, at doi:10.1016/j.agrformet.2024.110195.

References

Adams, S.B., Warren Jr, M.L., 2005. Recolonization by warmwater fishes and crayfishes after severe drought in upper coastal plain hill streams. Trans. Am. Fish. Soc. 134 (5), 1173–1192.
Alamri, S., et al., 2020. Silicon-induced postponement of leaf senescence is accompanied by modulation of antioxidative defense and ion homeostasis in mustard (Brassica juncea) seedlings exposed to salinity and drought stress. Plant Physiol. Biochem. 157, 47–59.
Anderson, M.C., et al., 2011. Evaluation of drought indices based on thermal remote sensing of evapotranspiration over the continental United States. J. Clim. 24 (8), 2025–2044.
Anderson, M.C., et al., 2016a. Relationships between the evaporative stress index and winter wheat and spring barley yield anomalies in the Czech Republic. Clim. Res. 70 (2–3), 215–230.
Anderson, M.C., Norman, J.M., Mecikalski, J.R., Otkin, J.A., Kustas, W.P., 2007. A climatological study of evapotranspiration and moisture stress across the continental United States based on thermal remote sensing: 2. surface moisture climatology. J. Geophys. Res. Atmos. 112 (D11).
Anderson, M.C., et al., 2016b. The Evaporative Stress Index as an indicator of agricultural drought in Brazil: an assessment based on crop yield impacts. Remote Sens. Environ. 174, 82–99.
Bachmair, S., Tanguy, M., Hannaford, J., Stahl, K., 2018. How well do meteorological indicators represent agricultural and forest drought across Europe? Environ. Res. Lett. 13 (3), 034042.
Barr, A., Morgenstern, K., Black, T., McCaughey, J., Nesic, Z., 2006. Surface energy balance closure by the eddy-covariance method above three boreal forest stands and implications for the measurement of the CO2 flux. Agric. For. Meteorol. 140 (1–4), 322–337.
Blackman, C.J., et al., 2016. Toward an index of desiccation time to tree mortality under drought. Plant Cell Environ. 39 (10), 2342–2345.
Bond, N.R., Lake, P.S., Arthington, A.H., 2008. The impacts of drought on freshwater ecosystems: an Australian perspective. Hydrobiologia 600, 3–16.
Bright, R.M., Miralles, D.G., Poyatos, R., Eisner, S., 2022. Simple models outperform more complex big-leaf models of daily transpiration in forested biomes. Geophys. Res. Lett. 49 (18), e2022GL100100.
Brown, J.F., Wardlow, B.D., Tadesse, T., Hayes, M.J., Reed, B.C., 2008. The vegetation drought response index (VegDRI): a new integrated approach for monitoring drought stress in vegetation. GIsci Remote Sens. 45 (1), 16–46.
Brzostek, E.R., et al., 2014. Chronic water stress reduces tree growth and the carbon sink of deciduous hardwood forests. Glob. Chang Biol. 20 (8), 2531–2539.
Christian, J.I., et al., 2021. Global distribution, trends, and drivers of flash drought occurrence. Nat. Commun. 12 (1), 6330.
Christian, J.I., et al., 2019. A methodology for flash drought identification: application of flash drought frequency across the United States. J. Hydrometeorol. 20 (5), 833–846.
Clapp, R.B., Hornberger, G.M., 1978. Empirical equations for some soil hydraulic properties. Water Resour. Res. 14 (4), 601–604.
Dai, Y., et al., 2019. A global high-resolution data set of soil hydraulic and thermal properties for land surface modeling. J. Adv. Model. Earth Syst. 11 (9), 2996–3023.
Duan, Q., Gupta, V.K., Sorooshian, S., 1993. Shuffled complex evolution approach for effective and efficient global minimization. J. Optim. Theory Appl. 76, 501–521.
Flo, V., Martinez-Vilalta, J., Steppe, K., Schuldt, B., Poyatos, R., 2019. A synthesis of bias and uncertainty in sap flow methods. Agric. For. Meteorol. 271, 362–374.
Gazol, A., Camarero, J., Anderegg, W., Vicente-Serrano, S., 2017. Impacts of droughts on the growth resilience of Northern Hemisphere forests. Global Ecol. Biogeogr. 26 (2), 166–176.
Gouveia, C., Trigo, R.M., Beguería, S., Vicente-Serrano, S.M., 2017. Drought impacts on vegetation activity in the mediterranean region: an assessment using remote sensing data and multi-scale drought indicators. Glob. Planet Change 151, 15–27.
Gu, C., et al., 2018. Partitioning evapotranspiration using an optimized satellite-based ET model across biomes. Agric. For. Meteorol. 259, 355–363.
Hargreaves, G.H., Samani, Z.A., 1985. Reference crop evapotranspiration from temperature. Appl. Eng. Agric. 1 (2), 96–99.
Hernandez-Santana, V., Hernandez-Hernandez, A., Vadeboncoeur, M.A., Asbjornsen, H., 2015. Scaling from single-point sap velocity measurements to stand transpiration in a multispecies deciduous forest: uncertainty sources, stand structure effect, and future scenarios. Can. J. For. Res. 45 (11), 1489–1497.
Hobbins, M.T., et al., 2016. The evaporative demand drought index. Part I: linking drought evolution to variations in evaporative demand. J. Hydrometeorol. 17 (6), 1745–1761.
Kool, D., et al., 2014. A review of approaches for evapotranspiration partitioning. Agric For Meteorol 184, 56–70.
Kustas, W.P., Norman, J.M., 1999. Evaluation of soil and vegetation heat flux predictions using a simple two-source model with radiometric temperatures for partial canopy cover. Agric. For. Meteorol. 94 (1), 13–29.
Li, X., et al., 2019. A simple and objective method to partition evapotranspiration into transpiration and evaporation at eddy-covariance sites. Agric. For. Meteorol. 265, 171–182.
Lin, C., et al., 2018. Diel ecosystem conductance response to vapor pressure deficit is suboptimal and independent of soil moisture. Agric. For. Meteorol. 250, 24–34.
Littell, J.S., Peterson, D.L., Riley, K.L., Liu, Y., Luce, C.H., 2016. A review of the relationships between drought and forest fire in the United States. Glob. Chang Biol. 22 (7), 2353–2369.
Liu, Y., Holtzman, N.M., Konings, A.G., 2021. Global ecosystem-scale plant hydraulic traits retrieved using model–data fusion. Hydrol. Earth Syst. Sci. 25 (5), 2399–2417.
Liu, Y., Kumar, M., Katul, G.G., Feng, X., Konings, A.G., 2020. Plant hydraulics accentuates the effect of atmospheric moisture stress on transpiration. Nat. Clim. Chang 10 (7), 691–695.
Liu, Y., et al., 2017. Increasing atmospheric humidity and CO2 concentration alleviate forest mortality risk. Proc. Natl. Acad. Sci. 114 (37), 9918–9923.
Lorenz, D.J., Otkin, J.A., Zaitchik, B., Hain, C., Anderson, M.C., 2021. Predicting rapid changes in evaporative stress index (ESI) and soil moisture anomalies over the continental United States. J. Hydrometeorol. 22 (11), 3017–3036.
McDowell, N., et al., 2008. Mechanisms of plant survival and mortality during drought: why do some plants survive while others succumb to drought? New Phytol. 178 (4), 719–739.
Meng, X., Evans, J., McCabe, M., 2014. The impact of observed vegetation changes on land–atmosphere feedbacks during drought. J. Hydrometeorol. 15 (2), 759–776.
Miralles, D.G., Gentine, P., Seneviratne, S.I., Teuling, A.J., 2019. Land–atmospheric feedbacks during droughts and heatwaves: state of the science and current challenges. Ann. N. Y. Acad. Sci. 1436 (1), 19–35.
Mitchell, P.J., Veneklaas, E., Lambers, H., Burgess, S.S., 2009. Partitioning of evapotranspiration in a semi-arid eucalypt woodland in south-western Australia. Agric. For. Meteorol. 149 (1), 25–37.
Monteith, J., 1965a. Evaporation and Environment In Symposia of the Society For Experimental Biology, 19. Cambridge University Press (CUP), Cambridge, pp. 205–234, 1965.
Monteith, J.L., 1965b. Evaporation and environment, Symposia of the Society For Experimental Biology. Cambridge University Press (CUP) Cambridge, pp. 205–234.
Nelson, J.A., et al., 2020. Ecosystem transpiration and evaporation: insights from three water flux partitioning methods across FLUXNET sites. Glob. Chang Biol. 26 (12), 6916–6930.
Nguyen, H., et al., 2019. Using the evaporative stress index to monitor flash drought in Australia. Environ. Res. Lett. 14 (6), 064016.
Niu, S., et al., 2014. Plant growth and mortality under climatic extremes: an overview. Environ. Exp. Bot. 98, 13–19.
Otkin, J.A., et al., 2013. Examining rapid onset drought development using the thermal infrared–based evaporative stress index. J. Hydrometeorol. 14 (4), 1057–1074.
Otkin, J.A., Anderson, M.C., Hain, C., Svoboda, M., 2014. Examining the relationship between drought development and rapid changes in the evaporative stress index. J. Hydrometeorol. 15 (3), 938–956.
Oudin, L., et al., 2005. Which potential evapotranspiration input for a lumped rainfall–runoff model?: part 2—towards a simple and efficient potential evapotranspiration model for rainfall–runoff modelling. J. Hydrol. 303 (1–4), 290–306.
Penman, H.L., 1948. Natural evaporation from open water, bare soil and grass. Proc. R. Soc. Lond. Ser. A. Math. Phys. Sci. 193 (1032), 120–145.
Perkins, S., Alexander, L., Nairn, J., 2012. Increasing frequency, intensity and duration of observed global heatwaves and warm spells. Geophys. Res. Lett. 39 (20).
Poyatos, R., et al., 2020. Global transpiration data from sap flow measurements: the SAPFLUXNET database. Earth Syst. Sci. Data Discuss. 2020, 1–57.
Poyatos, R. et al., 2019. SAPFLUXNET: a global database of sap flow measurements (0.1.3). Zenodo, https://doi.org/10.5281/zenodo.2530798.
Poyatos, R., et al., 2016. SAPFLUXNET: Towards a Global Database of Sap Flow Measurements. Oxford University Press, pp. 1449–1455.
Priestley, C.H.B., Taylor, R.J., 1972. On the assessment of surface heat flux and evaporation using large-scale parameters. Mon. Weather Rev. 100 (2), 81–92.
Raghav, P., Wagle, P., Kumar, M., Banerjee, T., Neel, J.P., 2022. Vegetation index-based partitioning of evapotranspiration is deficient in grazed systems. Water Resour. Res. 58 (8), e2022WR032067.
Rai, G.K., et al., 2021. Leaf proteome response to drought stress and antioxidant potential in tomato (Solanum lycopersicum L.). Atmosphere (Basel) 12 (8), 1021.
Ray, R.L., Fares, A., Risch, E., 2018. Effects of drought on crop production and cropping areas in Texas. Agric. Environ. Lett. 3 (1), 170037.
Reich, P.B., et al., 2018. Effects of climate warming on photosynthesis in boreal tree species depend on soil moisture. Nature 562 (7726), 263–267.

Ronda, R., De Bruin, H., Holtslag, A., 2001. Representation of the canopy conductance in modeling the surface energy budget for low vegetation. J. Appl. Meteorol. Climatol. 40 (8), 1431–1444.
Ross, I.U.k., Ross, J., 1981. The Radiation Regime and Architecture of Plant Stands. Springer Science & Business Media.
Saxton, K., Rawls, W.J., Romberger, J.S., Papendick, R., 1986. Estimating generalized soil-water characteristics from texture. Soil Sci. Soc. Am. J. 50 (4), 1031–1036.
Schumacher, D.L., Keune, J., Dirmeyer, P., Miralles, D.G., 2022. Drought self-propagation in drylands due to land–atmosphere feedbacks. Nat. Geosci. 15 (4), 262–268.
Scott, R.L., Biederman, J.A., 2017. Partitioning evapotranspiration using long-term carbon dioxide and water vapor fluxes. Geophys. Res. Lett. 44 (13), 6833–6840.
Sellers, P.J., Heiser, M.D., Hall, F.G., 1992. Relations between surface conductance and spectral vegetation indices at intermediate (100 m2 to 15 km2) length scales. J. Geophys. Res. Atmos. 97 (D17), 19033–19059.
Seneviratne, S., 2022. Weather and climate extreme events in a changing climate. IPCC Sixth Assessment Report.
Shuttleworth, W.J., Wallace, J., 1985. Evaporation from sparse crops-an energy combination theory. Q. J. R. Meteorolog. Soc. 111 (469), 839–855.
Stoy, P.C., et al., 2019. Reviews and syntheses: turning the challenges of partitioning ecosystem evaporation and transpiration into opportunities. Biogeosciences 16 (19), 3747–3775.
Sun, X., Wilcox, B.P., Zou, C.B., 2019. Evapotranspiration partitioning in dryland ecosystems: a global meta-analysis of in situ studies. J. Hydrol. 576, 123–136.
Suyker, A.E., Verma, S.B., 2010. Coupling of carbon dioxide and water vapor exchanges of irrigated and rainfed maize–soybean cropping systems and water productivity. Agric. For. Meteorol. 150 (4), 553–563.
Talsma, C.J., et al., 2018. Partitioning of evapotranspiration in remote sensing-based models. Agric. For. Meteorol. 260, 131–143.
Thornthwaite, C.W., 1948. An approach toward a rational classification of climate. Geogr. Rev. 38 (1), 55–94.
Ukkola, A.M., Abramowitz, G., De Kauwe, M.G., 2022. A flux tower dataset tailored for land model evaluation. Earth Syst. Sci. Data 14 (2), 449–461.
Unkovich, M., Baldock, J., Farquharson, R., 2018. Field measurements of bare soil evaporation and crop transpiration, and transpiration efficiency, for rainfed grain crops in Australia–a review. Agric. Water Manage. 205, 72–80.
Van Dijk, A.I., et al., 2013. The Millennium Drought in southeast Australia (2001–2009): natural and human causes and implications for water resources, ecosystems, economy, and society. Water Resour. Res. 49 (2), 1040–1057.
Vicente-Serrano, S.M., McVicar, T.R., Miralles, D.G., Yang, Y., Tomas-Burguera, M., 2020. Unraveling the influence of atmospheric evaporative demand on drought and its response to climate change. Wiley Interdiscip. Rev. Clim. Change 11 (2), e632.
Wagle, P., Raghav, P., Kumar, M., Gunter, S.A., 2023. Influence of water use efficiency parameterizations on flux variance similarity-based partitioning of evapotranspiration. Agric. For. Meteorol. 328, 109254.
Wei, Z., Lee, X., Wen, X., Xiao, W., 2018. Evapotranspiration partitioning for three agro-ecosystems with contrasting moisture conditions: a comparison of an isotope method and a two-source model calculation. Agric. For. Meteorol. 252, 296–310.
Wei, Z., et al., 2017. Revisiting the contribution of transpiration to global terrestrial evapotranspiration. Geophys. Res. Lett. 44 (6), 2792–2801.
Xu, Z., et al., 2013. Intercomparison of surface energy flux measurement systems used during the HiWATER-MUSOEXE. J. Geophys. Res. Atmos. 118 (23), 157, 13,140-13.
Yang, X., Wang, B., Chen, L., Li, P., Cao, C., 2019. The different influences of drought stress at the flowering stage on rice physiological traits, grain yield, and quality. Sci. Rep. 9 (1), 3742.
Yang, Y., et al., 2021. Studying drought-induced forest mortality using high spatiotemporal resolution evapotranspiration data from thermal satellite imaging. Remote Sens. Environ. 265, 112640.
Zahn, E., et al., 2022. Direct partitioning of eddy-covariance water and carbon dioxide fluxes into ground and plant components. Agric. For. Meteorol. 315, 108790.
Zamuda, C., et al., 2013. US Energy Sector Vulnerabilities to Climate Change and Extreme Weather. US Department of Energy. https://energy.gov/sites/prod/files/2013/07/f2/20130716-Energy%20Sector%20Vulnerabilities%20Report.pdf.
Zeng, Z., et al., 2023. Increased risk of flash droughts with raised concurrent hot and dry extremes under global warming. npj Clim. Atmos. Sci. 6 (1), 134.
Zhou, S., Yu, B., Zhang, Y., Huang, Y., Wang, G., 2016. Partitioning evapotranspiration based on the concept of underlying water use efficiency. Water Resour. Res. 52 (2), 1160–1175.